

## Investigation of the vortex instability in a two-dimensional inkjet print-zone using numerical analysis

A. F. V. de A. Aquino <sup>1,2,\*</sup>, S. G. Mallinson <sup>1,2</sup>, G. D. McBain <sup>2</sup>, G. D. Horrocks <sup>2</sup>,  
C. M. de Silva,<sup>1</sup> and T. J. Barber <sup>1</sup>

<sup>1</sup>*School of Mechanical and Manufacturing Engineering University of New South Wales,  
Sydney NSW 2052, Australia*

<sup>2</sup>*Memjet, Macquarie Park NSW 2113, Australia*



(Received 2 March 2021; accepted 22 November 2021; published 28 January 2022)

A numerical model was employed to investigate the vortex instability in a two-dimensional inkjet print-zone. The simulation models the entrainment effect of the droplets on the airflow via a dispersed-phase continuum method that, due to the separation of length scales, treats the force exerted by the main droplets as a continuum smooth field. The trajectory and speed of the main droplets are also assumed to be unaffected by the airflow. The results indicate the existence of a dimensionless droplet density threshold ( $N_c$ ) at which the vortex shifts from steady to oscillatory. This demonstrates that the two-dimensional instability has a supercritical Hopf type of bifurcation, i.e., the shift from stable to unstable is continuous but not smooth and the amplitude of oscillation follows the asymptotic square-root behavior characteristic of this type of bifurcation. Further, as shown by tests with stationary paper and no induced cross-flow, the mechanism of instability cannot be attributed to the interaction between the incoming cross-flow and the entrained airflow. Characterizing the two-dimensional airflow instabilities and their mechanism provides a better understanding of the airflow dynamics in the print gap of inkjet printers.

DOI: [10.1103/PhysRevFluids.7.013904](https://doi.org/10.1103/PhysRevFluids.7.013904)

### I. INTRODUCTION

Inkjet printers deposit ink droplets onto a substrate in predefined positions, creating a two-dimensional pattern. Due to the easy control of the printing pattern and the repeatability of the process, the use of inkjet printers is no longer limited to graphics applications and has been expanded to manufacturing electronics, solar panels, rapid prototypes, and reinforced composites [1–3]. In these applications, fine features with resolution of tenths of millimeters are reproduced, which demands highly accurate deposition of droplets on the substrate [3].

The expansion of inkjet technology to other applications, or even further within the graphics sector, remains limited by the restrictive print height ( $H$ ) with which inkjet printers can operate (Fig. 1). Specifically, small print gaps prevent the printer from accommodating media with variable or large thickness and increase the likelihood of the media striking the printhead, which can damage the nozzles, demanding expensive maintenance. At high print heights, however, the print quality is likely to be compromised due to the misplacement of droplets which tends to create printing defects [4–10].

These printing defects have been linked to specific aerodynamic effects that influence droplets trajectories [5,8,9,11]. The airflow in the print gap is formed by an interaction between the cross-flow and the induced impinging air-jet (Fig. 1), which is created by the droplets motion in an effect

\*andre.aquino@unsw.edu.au

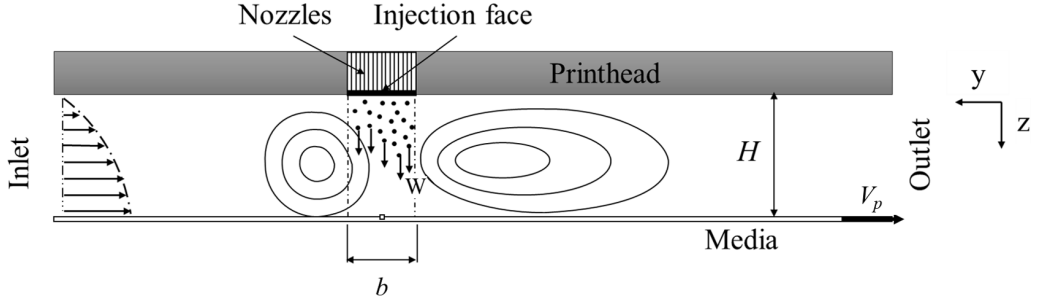


FIG. 1. Schematic of the physics in the print gap, where  $H$  is the print gap height,  $W$  is the droplet velocity,  $V_p$  is the paper speed,  $b$  is the breadth of the print-zone, and the origin of the coordinate system is marked by the white square.

named here as airflow entrainment. Satellite droplets, due to their lower Stokes numbers ( $S < 1$ ), are likely to be carried by the airflow, landing away from main droplets ( $S > 10$ ), where the Stokes number is defined by Eq. (1):

$$S = \frac{\rho_d d^2 |W - V_p|}{18\mu H}, \quad (1)$$

where  $\rho_d$  is the droplet density,  $d$  is the diameter of the droplet,  $\mu$  is the dynamic viscosity of air,  $W$  is the droplet ejection velocity, and  $V_p$  is the paper speed. When the airflow oscillates at larger print gaps ( $H < 1$  mm), the satellites are periodically misplaced on the paper [5–7]. At scenarios of large unsteadiness, the main droplet can also be periodically misplaced [10], but this regime is already beyond the envelope that defines a functional printer.

Link *et al.* [11] had initially proposed that droplet misplacement was created by vortices induced by the forward-facing step of the printhead geometry. However, numerical simulations and particle image velocimetry (PIV) experiments conducted in their study [11] refuted this hypothesis as the vortices minimally affected the mean airflow in the print gap. The study of Lanzerstorfer and Kuhlmann [12] on the forward-facing step also confirmed that the airflow is asymptotically stable for Reynolds numbers below 680. Other works using time-resolved PIV [9] measurements and particle-in-cell tracking simulations [5,13] have highlighted that printing defects can be a result of the oscillation of the vortices created by the entrainment effect. They reported that, at specific operating conditions, the airflow becomes three-dimensional and the vortices become unstable, inducing a periodic misplacement of droplets on the paper.

While it has been demonstrated that the vortices tend to oscillate at low volumetric flow rate across the print-zone (low paper speed and/or low downstream suction) and high droplet mass flux [5–10,13], little is known about the dynamics of the oscillation. Furthermore, the vortex instability has also been linked to the interaction between the incoming cross-flow and the entrained airflow, but there is evidence to challenge this assertion because laminar impinging jets of air can develop a self-sustained oscillation even when there is no cross-flow [14–16]. Varieras *et al.* [14] indicated that the self-sustained oscillation of a laminar impinging plane jet of air is characterized by a two-dimensional mode of oscillation that presents a supercritical Hopf bifurcation [17]. The natural frequency of oscillation of the impinging plane jet increases as the jet speed increases and the confinement height ( $H$ ) decreases. Due to some physical similarities of the problems, it is expected that the entrained airflow in the print gap will present similar behavior.

We note, the base flow that creates uniform prints without tiger stripe or wood grain is expected to be homogeneous in time and the span direction. Based on that, two-dimensional numerical analyses are performed to shed light into the dynamics of the vortex in the print-zone and determine the range of flow regimes at different conditions. This will provide a refined understanding of the

two-dimensional mode of oscillation while characterizing the upper bound at which the base flow meets the conditions for a uniform print. Tests are also conducted to determine whether the interaction between the incoming cross-flow and the entrained airflow triggers the instability.

## II. METHODOLOGY

### A. Numerical model

The OPENFOAM solver PIMPLEFOAM is used to solve the governing equations for incompressible flows:

$$\frac{\partial \mathbf{u}}{\partial t} + \mathbf{u} \cdot \nabla \mathbf{u} = -\frac{1}{\rho} \nabla p + \mathbf{F}(\mathbf{U} - \mathbf{u}) + \nu \nabla^2 \mathbf{u}, \quad (2)$$

$$\nabla \cdot \mathbf{u} = 0, \quad (3)$$

where  $\mathbf{u}$  is the velocity field,  $t$  is time,  $p$  is pressure,  $\nu$  is the air kinematic viscosity, and  $\mathbf{F}$  is the body force induced by the point particles (main droplets) moving at velocity  $\mathbf{U}$ .

The force exerted by the droplets is equal but of opposite sign to the drag the droplets experience, which is of the form of Stokes's drag law with an empirical correction factor  $(1 + \varphi)$  [Eq. (5)]. The empirical factor used here was calculated using Eq. (4) as White and Corfield defined it [18, Eq. (3–225)] and comes from a fit to experimental data for droplet Reynolds number lower than 200 000. This covers the range of droplet Reynolds number ( $Re_d$ ) tested in this paper, which is approximately  $4.5 < Re_d < 16$ . Here, the Reynolds number is given by  $Re_d = \frac{|W\mathbf{k} - \mathbf{u}|d}{\nu}$ , where  $\mathbf{k}$  is the unit vector in the  $z$  direction and  $W\mathbf{k} = \mathbf{U}$ . The Reynolds number for the flow across the print gap, on the other hand, is given by  $Re_H = \frac{V_p H}{\nu}$  and varies from 0 to 250:

$$\varphi(Re_d) = \frac{Re_d}{4(1 + \sqrt{Re_d})} + \frac{Re_d}{60}. \quad (4)$$

Previous studies [5,13] have modeled the droplets using the classic particle-in-cell (Lagrangian) method, which employs additional kinematic equations to track the droplets and, as a result, demands higher computational cost. Therefore, to prevent this additional computational cost, a dispersed-phase continuum (DPC) method is implemented in this paper. This model assumes that, due to the separation of length scales (droplet diameter, droplet spacing, droplet wake length, and airflow structure size), the dispersed phase can be treated as a continuum. This results in  $\mathbf{F}$  being a smooth continuous field given by Eq. (5). Here,  $n$  is the number density or number of droplets per unit volume in the predefined print-zone (Fig. 1) and depends on the number of nozzles per unit area on the injection face ( $\sigma$ ), the firing frequency ( $f_n$ ), and the droplet speed ( $W$ ) [Eq. (6)]. It is also assumed here that the main droplets have constant speed and, due to their high Stokes number, their trajectories are unaffected, as indicated in previous studies [5,8,11,13]. The DPC method takes approximately half of the time that the particle-in-cell method takes to calculate the same solution:

$$\mathbf{F} = 3\pi \nu n d (\mathbf{U} - \mathbf{u}) (1 + \varphi), \quad (5)$$

$$n = \frac{\sigma f_n}{W}. \quad (6)$$

To couple the pressure and momentum equations, the PIMPLE scheme [19] is employed here due to its robustness. It is deemed that the outer loop of the PIMPLE scheme has reached convergence when the pressure and momentum residuals fall to less than  $10^{-5}$ , as suggested by Holzmann [19]. Pure Crank-Nicolson, a second-order implicit scheme, is used to discretize the time derivative, while the second-order discretization of the gradient, divergence, and Laplacian terms is achieved via the unbounded central differencing algorithm, named Gauss linear in the OPENFOAM idiom [19]. The velocity terms are solved using the biconjugate gradient method with a diagonal incomplete

lower-upper (LU) preconditioner [20], whereas the geometric algebraic multigrid method is used to solve the pressure equation, with diagonal incomplete Cholesky–Gauss-Seidel smoothing [21].

The transient simulations are initialized using a steady-state solution of the entrained airflow calculated using the SCIKIT-FEM [22] finite element method of the PYTHON library. The code has been chosen as it provides greater numerical stability than the OPENFOAM steady-state solver at conditions where the flow is unstable. This higher stability is achieved by implementing the Newton iteration method [23] and numerical continuation [17]. The flow field computed by SCIKIT-FEM is projected into the transient simulation, serving as the initial time step ( $t = 0$  s).

## B. Boundary conditions

Both the inlet and outlet in SCIKIT-FEM are set as open boundaries, whereas the inlet in OPENFOAM is set with zero pressure gradient and a velocity profile that has been captured at the inlet of the SCIKIT-FEM simulations and the outlet has zero gauge pressure. The paper is modeled as a moving wall with no slip, traveling at a speed  $V_p$ , while the printhead is a stationary wall with no slip. The droplets have an ejection velocity of 14.95 m/s and are assumed to be solid spheres with diameter of 15.6  $\mu\text{m}$ . The droplet diameter and velocity were estimated experimentally by measuring the average ejected mass of several thousand droplets using an accurate balance, and from high magnification stroboscopic imaging of the ejection process, respectively.

## C. Geometry

A rectangular domain is created to model the print gap defined by the printhead and the media (Fig. 1). The domain has the same length as a printhead system, with the inlet and outlet, respectively, located at 25 mm upstream and 45 mm downstream. These are, respectively, where the leading and trailing edge of the printhead are located. The model, however, simplifies the problem by using a flat roof.

A schematic of the problem is shown in Fig. 1, where ink droplets are fired from the injection face into the injection zone which has length  $b$  and extends from  $-0.5$  to  $0.5$  mm. The coordinate system orientation arises from the perspective of the printed image on the paper: the media is located at  $z = 0$  and the print nozzles are located at  $z = -H$ , thus the nozzles fire in the positive  $z$  direction. When the printed image is viewed from above, the paper moves downward, which is equivalent to the negative  $y$  direction in Fig. 1.

## D. Spatial and temporal discretization

The domain is discretized using a structured mesh created in OPENFOAM. A uniform mesh with a cell size of 0.022mm is employed from  $y = -1.5$  to 2.5 mm to ensure a high resolution in the region of interest near the print-zone. Upstream and downstream of this region, geometric growth rates of 1.05 and 1.03, respectively, are implemented in the  $y$  direction to reduce the cell count and the computational cost. This results in a mesh with over 58 000 cells when  $H = 3$  mm, which represents 1/3 of the cell count of a uniform mesh with a cell size of 0.022 mm.

In an earlier grid independence study [7], the difference in the amplitude of oscillation of the velocity magnitude, when refining the mesh from a case with a uniform cell size of 0.022 to 0.0148 mm, is approximately 2.33% and the grid convergence index error between these two refinement levels is equal to 0.94%. The amplitude observed using the nonuniform mesh created here, in comparison to the uniform mesh, only differs by 1%, which is deemed as acceptable.

For the SCIKIT-FEM mesh, a similar strategy is implemented, with the difference that the cell size around the injection zone is equal to 0.033 mm. This is done because the velocity magnitude computed by SCIKIT-FEM only varies by less than 1% when the cell size is refined to 0.022 mm. Furthermore, due to the use of direct solvers in the SCIKIT-FEM code, further mesh refinements make the computational cost of the simulations unfeasible.

A time step of  $5 \times 10^{-6}$  s is set in the simulations, which results in a maximum Courant number of approximately 1.3. The previous verification study [7] indicated that the amplitude of velocity oscillation varies only by 2.4% when the time step decreases to  $1 \times 10^{-6}$  s while increasing the computational cost by over five times.

### E. Nondimensionalizing the print-zone

Equation (2) is nondimensionalized using the ejection droplet speed  $W$ , and the print gap height  $H$  as the characteristic scales. The corresponding derived scale for time is the transit time  $H/W$ , while for pressure it is  $\rho W^2$ , which gives the nondimensionalized Navier-Stokes equation:

$$\frac{\partial \tilde{\mathbf{u}}}{\partial \tilde{t}} + \tilde{\mathbf{u}} \cdot \nabla \tilde{\mathbf{u}} = -\frac{1}{\rho} \nabla \tilde{p} - 3\pi N(\tilde{\mathbf{u}} + \mathbf{k})(1 + \phi) + R^{-1} \nabla^2 \tilde{\mathbf{u}}, \quad (7)$$

where  $\tilde{\mathbf{u}}$ ,  $\tilde{p}$ , and  $\tilde{t}$  are the normalized  $\mathbf{u}$  and  $p$ ,  $t$ ;  $N$  is the dimensionless number density of drops given by  $N = ndHv/W$  and  $R$  represents the transit Reynolds number given by  $R = HW/v$ . The additional governing dimensionless parameters are the dimensionless print gap height or aspect ratio ( $b/H$ ), where  $b$  is the breadth of the print-zone, and the dimensionless droplet diameter ( $d/H$ ).

## III. RESULTS

### A. Characterizing the airflow instability

The flow regimes and the instability are characterized by measuring the airflow response for a matrix of cases defined by different number densities. The different number densities are set with variations in the number of nozzles firing droplets per unit area ( $\sigma$ ) which affects the optical density of the colored figure printed on the paper. This section investigates a case with  $V_p/W = 0.027$ ,  $b/H = 1/3$ , and  $f_n = 15.5$  kHz in an attempt to reproduce the conditions that the market currently demands. The velocity and vorticity fields for a case with  $N = 1.57 \times 10^{-3}$  exhibit two main counter-rotating vortices near the injection zone. These vortices are created by a similar mechanism as observed in impinging jets. The relative motion between droplets and surrounding air induces an impinging air-jet and this induced air-jet hits the media over an impact zone, where the axial momentum is converted through pressure into radial momentum. This leads to strong lateral velocities in the vicinity of the media. The low-pressure region near the injection face sucks the surrounding air back into the impinging airflow, completing the recirculation loop and forming two vortices.

Due to the incoming cross-flow induced by the paper motion, the upstream and downstream vortices are distorted. The incoming cross-flow causes the upstream vortex to be compact and have a stronger core due to the higher rate at which axial momentum is converted into radial momentum; the downstream vortex is stretched, becoming weaker. At the bottom of the upstream vortex, a region of positive vorticity is created as the fluid layer adjacent to the paper moves in the negative  $y$  direction while the bottom part of the upstream vortex moves in the positive  $y$  direction, indicating the existence of a small clockwise vortex. At the bottom of the downstream vortex, a negative vorticity region is observed even though the adjacent fluid layers move in the same direction. This is because the bottom part of the downstream vortex has a higher horizontal velocity than that of the paper.

The time snapshots show the nonsteady behavior of the entrained airflow (Fig. 2), where both upstream and downstream vortices present an unstable and periodic oscillation. This would likely cause periodic misplacement of droplets on the media in practical systems. Due to the airflow oscillation in the wake of the downstream vortex, it is believed that those droplets that stay in suspension (mist) far downstream of the injection zone can have their trajectories affected by the wake oscillation, leading to further misdeposition on the paper, as indicated in Rodriguez-Rivero *et al.* [9].

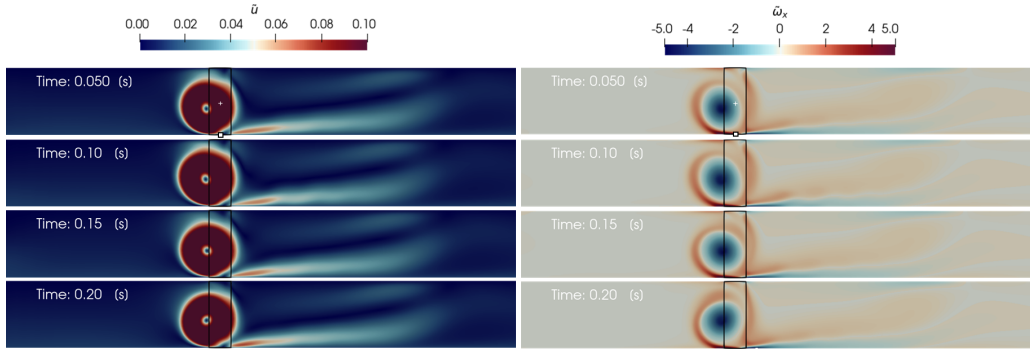


FIG. 2. Nondimensionalized velocity magnitude ( $\tilde{u} = u/W$ ) and planar vorticity ( $\tilde{\omega}_x = \omega_x H/W$ ) fields:  $b/H = 1/3$ ,  $N = 1.57 \times 10^{-3}$ , and  $V_p/W = 0.027$  where the white square represents the origin of the coordinate system and the white cross represents the probe location.

A probe is positioned near the region of maximum variation in velocity in the upstream vortex,  $z/H = -0.5$  mm and  $y/H = 0$ , to capture the velocity oscillation (Fig. 3). The measured velocity indicates three phases: the first where the flow develops from a steady equilibrium to a transient state, the second where the oscillation exponentially grows, and the last where the oscillation has fully developed at about 0.075 s, where the velocity magnitude reaches a maximum amplitude of  $6.71 \times 10^{-3}$ . The discrete Fourier transform (DFT) shows a spectrum composed of harmonics (see Fig. 4). Here, the frequency of oscillation,  $f$ , is presented in terms of the Strouhal number,  $St = fH/W$ . The first peak indicates the fundamental frequency or first harmonic, with  $St = 0.106$ , while the other frequencies are simple harmonics defined by an integer multiple of the fundamental frequency.

The case of  $N = 1.33 \times 10^{-3}$ , Fig. 5, shows that the two main recirculation zones are less evident than at higher number density values. This is a result of fewer droplets being fired into the injection zone, which leads to a lower transfer of momentum from the droplets to the surrounding air. This lower body-force induces a small oscillation in the flow field as indicated by the time snapshots (Fig. 5) and further confirmed by the plots of velocity oscillation (Fig. 6).

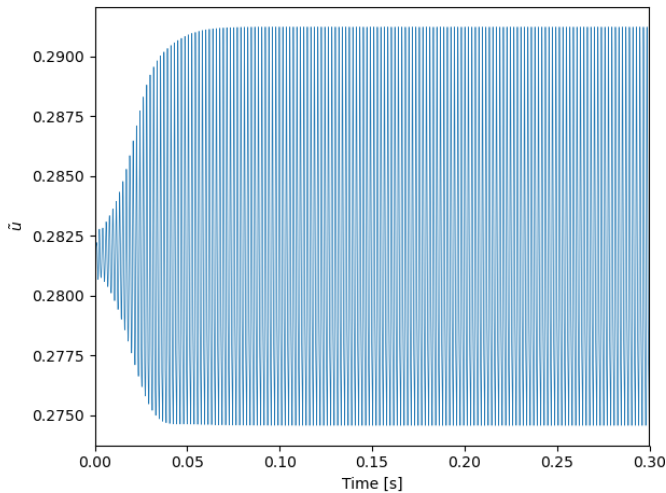


FIG. 3. Nondimensionalized velocity ( $\tilde{u} = u/W$ ) oscillation signal:  $b/H = 1/3$ ,  $N = 1.57 \times 10^{-3}$ , and  $V_p/W = 0.027$ .

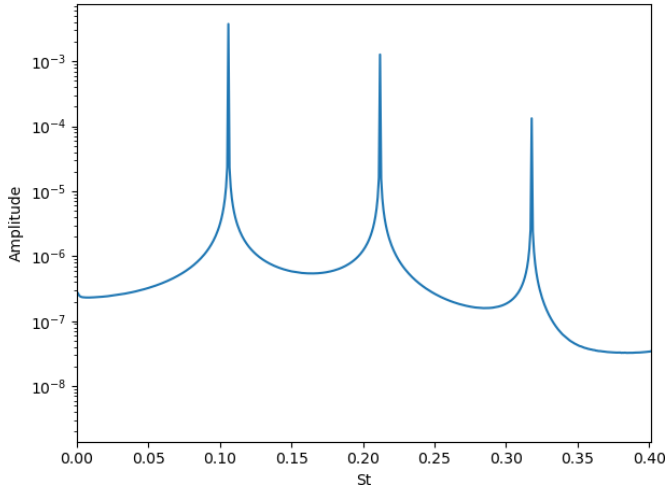


FIG. 4. Discrete Fourier transform of the case with  $b/H = 1/3$ ,  $N = 1.57 \times 10^{-3}$ , and  $V_p/W = 0.027$ .  $St = fH/W$ , where  $f$  is the frequency of oscillation.

The amplitude of velocity oscillation only reaches a value of  $3.75 \times 10^{-3}$ , which represents a reduction of approximately 50% compared to the value computed with  $N = 1.57 \times 10^{-3}$ . The flow takes approximately 0.2 s to reach a converged amplitude of oscillation, which is 0.125 s longer than the case with higher number density. The airflow also oscillates with a dominant frequency  $St = 0.104$  and the fundamental mode of oscillation has an amplitude one order of magnitude higher than the second harmonic. The predominant mode of oscillation has a practical importance as it directly determines the main length scale of print defects, which can significantly affect the severity of the problem since the human perception of the printing defect depends on the eye sensitivity to different length scales.

The case with  $N = 0.31 \times 10^{-3}$  shows that the main vortices are significantly weaker and the rotational field of the downstream vortex is barely observable (Fig. 7). Due to the reduction in the vorticity magnitude of the two main recirculation regions, a secondary flow feature is observed. Ridges in the vorticity field near the edges of the injection zone are seen and indicate the sharp variation in velocity that the flow experiences, caused by the motion of droplets.

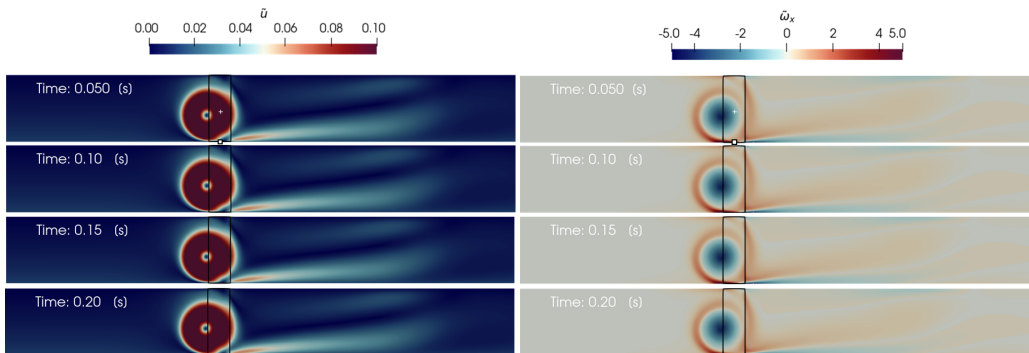


FIG. 5. Nondimensionalized velocity magnitude ( $\tilde{u} = u/W$ ) and planar vorticity ( $\tilde{\omega}_x = \omega_x H/W$ ) fields:  $b/H = 1/3$ ,  $N = 1.33 \times 10^{-3}$ , and  $V_p/W = 0.027$  where the square represents the origin of the coordinate system and the white cross represents the probe location.

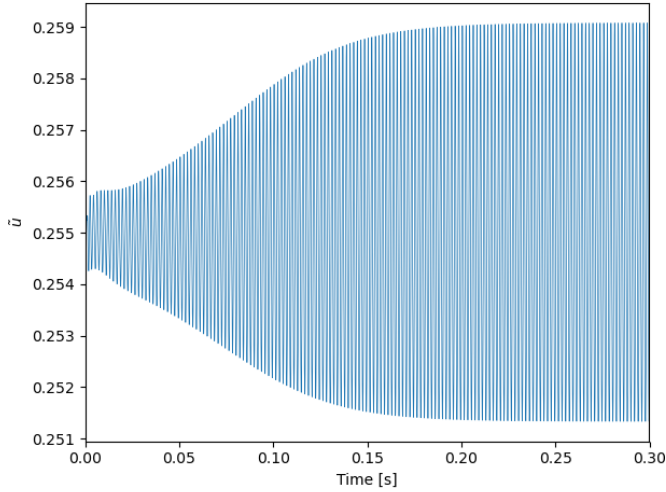


FIG. 6. Nondimensionalized velocity ( $\tilde{u} = u/W$ ) oscillation signal:  $b/H = 1/3$ ,  $N = 1.33 \times 10^{-3}$ , and  $V_p/W = 0.027$ .

The time snapshots indicate that the flow field is stable and, as a result, the droplet misplacement should not occur. This is further confirmed by the probe signal as no oscillation in velocity is measured over the 0.3 s of simulation. The steady behavior of this case indicates that there is a critical number density, higher than  $N = 0.31 \times 10^{-3}$  and lower than  $N = 1.33 \times 10^{-3}$ , at which the flow transitions from stable to unstable. The square of the amplitude of oscillation ( $\tilde{r}^2$ ) versus the number density plot (Fig. 8) shows the range of the flow regimes—stable and unstable—when the paper is moving at  $V_p/W = 0.027$ . Above a critical printing density ( $N_c \approx 1.30 \times 10^{-3}$ ), the airflow induced by the droplets motion develops a self-sustainable oscillation with a saturated amplitude, characterizing the supercritical Hopf bifurcation type of instability [17,24]. For any number density lower than  $N_c$ , the final solution is stable and steady and any small initial perturbation is dampened to reach a zero-amplitude equilibrium. Figure 8 indicates that for print densities larger than  $N_c$ , the square of the amplitude grows linearly as the number density is increased. This linear correlation can be approximated by the following equation:  $r^2 = 0.529N - 0.0007$  where the root ( $\tilde{r}^2 = 0$ ) represents the estimated critical number density and the slope is equal to  $(\frac{-1}{\alpha})$  where  $\alpha$  is the first

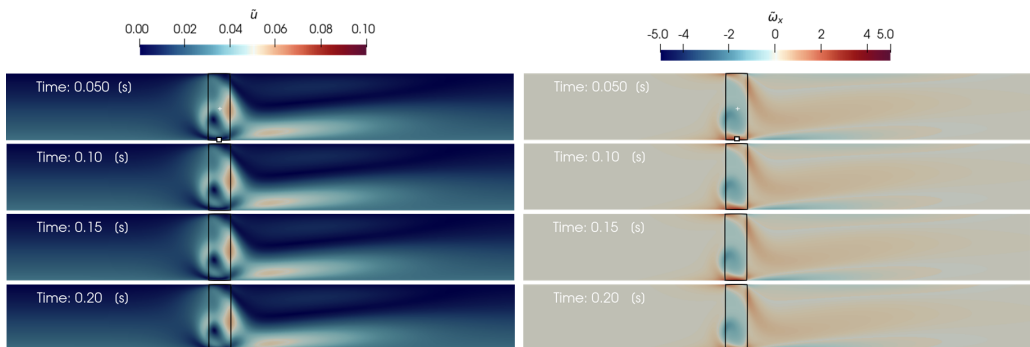


FIG. 7. Nondimensionalized velocity magnitude ( $\tilde{u} = u/W$ ) and planar vorticity ( $\tilde{\omega}_x = \omega_x H/W$ ) fields:  $b/H = 1/3$ ,  $N = 0.31 \times 10^{-3}$ , and  $V_p/W = 0.027$  where the square represents the origin of the coordinate system and the white cross represents the probe location.

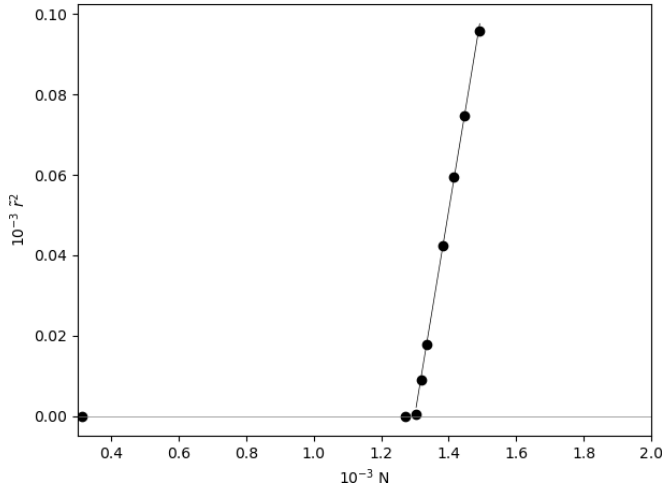


FIG. 8. Bifurcation diagram for  $V_p/W = 0.027$  and  $b/H = 1/3$ . Top figure: Nondimensional amplitude of oscillation ( $\bar{r}^2 = r^2/W^2$ ) vs dimensionless number density ( $N$ ). Bottom figure: Initial dimensionless velocity ( $\tilde{u}_0 = u_0/W$ ) vs number density ( $N$ ).

Lyapunov coefficient. Therefore, the estimated critical number density is  $1.32 \times 10^{-3}$  and  $\alpha$  is equal to  $-1.89$ .

Figure 9 indicates that there is a small increase in frequency due to increments in number density, but all fundamental frequencies hover around  $0.103$ – $0.106$  and the harmonics are multiple integers of the fundamental. Further, it is observed that the amplitude of the harmonics decreases as the number density reduces. The amplitude of the higher harmonics shows a more evident decay while the amplitude of the fundamentals experiences a more subtle reduction.

The airflow instability has been characterized by fluctuations in the flow field linked to the oscillation of the main vortices near the print-zone. The oscillation shows an exponential growth in a first stage until it develops to a saturated amplitude. This oscillation is further characterized by

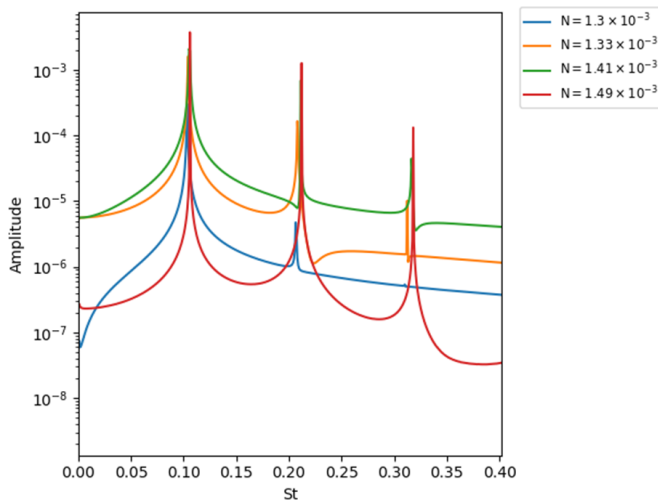


FIG. 9. Discrete Fourier transform for cases  $N = 1.3 \times 10^{-3}$ ,  $N = 1.33 \times 10^{-3}$ ,  $N = 1.41 \times 10^{-3}$ , and  $N = 1.49 \times 10^{-3}$ .

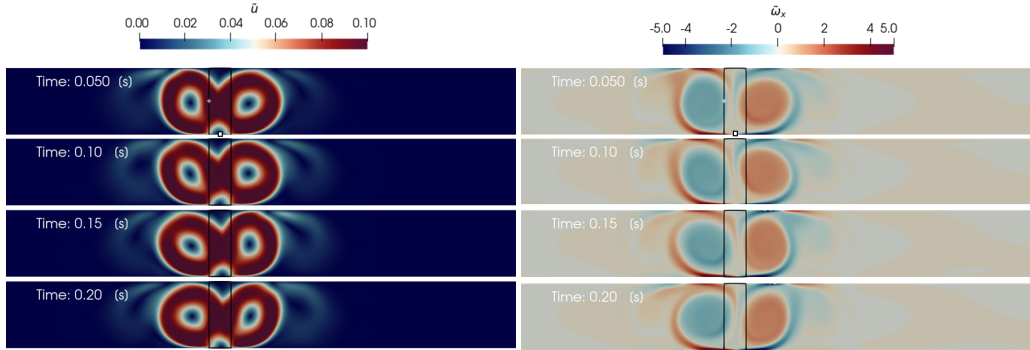


FIG. 10. Nondimensionalized velocity magnitude ( $\tilde{u} = u/W$ ) and planar vorticity ( $\tilde{\omega}_x = \omega_x H/W$ ) fields:  $b/H = 1/3$ ,  $N = 1.57 \times 10^{-3}$ , and  $V_p/W = 0$  where the square represents the origin of the coordinate system and the white cross represents the probe location.

a fundamental mode of oscillation and its harmonics. While the fundamental mode of oscillation is linked to the supercritical Hopf bifurcation, the higher harmonics arise from the nonlinearity of the governing Navier-Stokes equation.

### B. Influence of paper speed and induced incoming cross-flow

To investigate whether the onset of instability is triggered by the interaction between the induced cross-flow and the entrained airflow, as previous studies indicated in [5,13], a test with a stationary lower surface ( $V_p/W = 0$ ) is performed, with  $b/H = 1/3$  and  $N = 1.57 \times 10^{-3}$ . A following test with  $V_p/W = 0.041$  is also conducted to investigate the impact of higher paper speeds on the stability of the airflow and on the instability bifurcation.

The time snapshots indicate that even though there is no induced cross-flow, the entrained airflow becomes unstable (Fig. 10). Due to the lack of cross-flow, two counter-rotating symmetrical vortices are created which oscillate at the same frequency but with a phase delay. In contrast to the cases with moving paper, the oscillation propagates from the injection zone to the inlet and the outlet. The velocity vectors overlaid on the contour of  $x$  vorticity show that the impinging airflow creates two counter-rotating vortices (A), and also induces secondary recirculation cells (B) (Fig. 11). These cells are a result of the main vortices forcing the adjacent layer of fluid to move along with them and the wall blockage (top and bottom surfaces) transforming linear momentum into angular momentum. These secondary zones propagate throughout the whole domain but become weaker as they move away from the injection zone as the velocity difference between adjacent layers decreases. Similar flow features can also be observed when the paper is moving, but they are less evident due to the incoming cross-flow.

The velocity signal captured by a probe located at  $y/H = -0.5/3$  and  $z/H = -0.5$  indicates that the instability takes approximately 0.075 s to develop a saturated amplitude of  $9.69 \times 10^{-3}$  (Fig. 12).

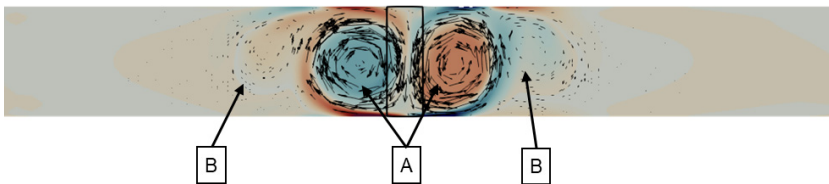


FIG. 11. System of vortices created by the entrained flow: main vortices (A) and secondary recirculation regions (B).

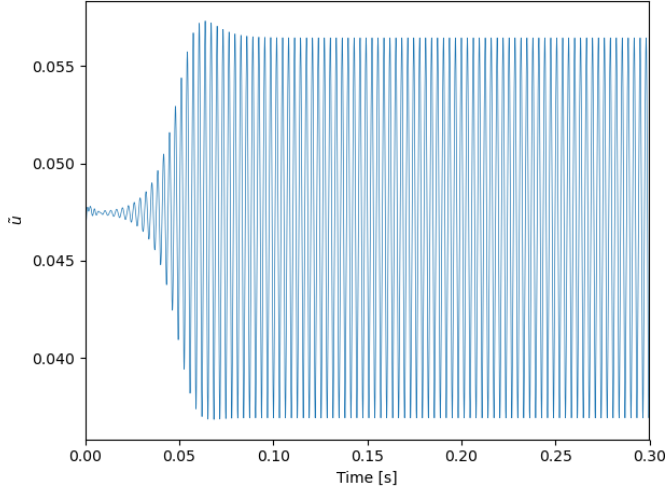


FIG. 12. Nondimensionalized velocity ( $\tilde{u} = u/W$ ) oscillation signal:  $b/H = 1/3$ ,  $N = 1.57 \times 10^{-3}$ , and  $V_p/W = 0$ .

The DFT identified that the first three harmonics have Strouhal number equal to 0.062, 0.124, and 0.186 and the first harmonic is the predominant frequency of oscillation. The instability regime for a stationary paper is defined by  $r^2 = 0.2316N - 0.00027$  (Fig. 13). The estimated critical number density is equal to  $N_c = 1.16 \times 10^{-3}$  and  $\alpha$  is equal to  $-4.32$ . This indicates that the amplitude increases at a lower rate than when the paper is moving.

When the paper speed increases to  $V_p/W = 0.041$  but  $H/b$  and  $N$  are kept constant, we can observe that the flow field becomes stable (Fig. 14). The downstream vortex becomes more stretched and the upstream vortex becomes smaller in comparison to the cases with lower paper speed. The large variation in velocity over a smaller area results in higher vorticity for the upstream vortex. The velocity signal measured by a probe at  $y/H = 0.5$  and  $z/H = -0.5$  showed that the initial oscillation is completely dampened out to converge into a steady-state flow within the 0.06 s of simulation.

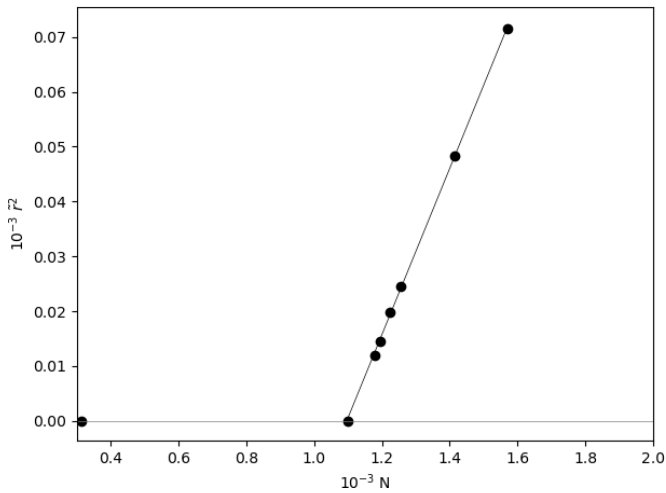


FIG. 13. Bifurcation diagram: Nondimensionalized amplitude of oscillation ( $\tilde{r}^2 = r^2/W^2$ ) vs dimensionless number density ( $N$ ) for  $V_p/W = 0$  and  $b/H = 1/3$ .

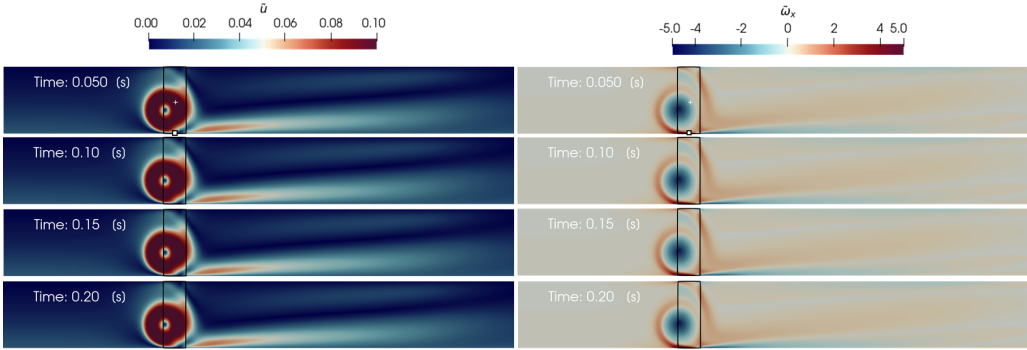


FIG. 14. Nondimensionalized velocity magnitude ( $\tilde{u} = u/W$ ) and planar vorticity ( $\tilde{\omega}_x = \omega_x H/W$ ) fields:  $b/H = 1/3$ ,  $N = 1.57 \times 10^{-3}$ , and  $V_p/W = 0.041$  where the white square represents the origin of the coordinate system and the white cross represents the probe location.

The bifurcation diagram for  $V_p/W = 0.041$  and  $b/H = 1/3$  (Fig. 15) shows that the transition occurs near a number density of  $N = 1.69 \times 10^{-3}$ . The instability regime near the onset of instability is defined by  $r^2 = 1.71N - 0.0029$ , which results in a critical number density equal to  $N_c = 1.7 \times 10^{-3}$  and  $\alpha$  equal to  $-0.585$ . In contrast to the stationary paper scenario that presented a higher  $\alpha$ , this lower  $\alpha$  suggests that the shift in stability is more sensitive to variations in number density.

Previous studies had indicated that the paper speed modulates the flow stability [1,5,6,9]. This is further confirmed by the results presented here, which also suggest that the critical number density tends to be higher at higher paper speeds. This is believed to be related to the higher cross-flow that creates a stabilizing effect on the vortices as suggested by Mallinson *et al.* [5,6].

### C. Influence of print gap height

Two sets of tests are conducted here to investigate the influence of print gap height on the stability of the airflow. The first set of tests has a print gap height of  $b/H = 1/3.3$ , while the second one has  $b/H = 1/3.6$ . Both tests are conducted with  $V_p/W = 0.041$ . The bifurcation diagram

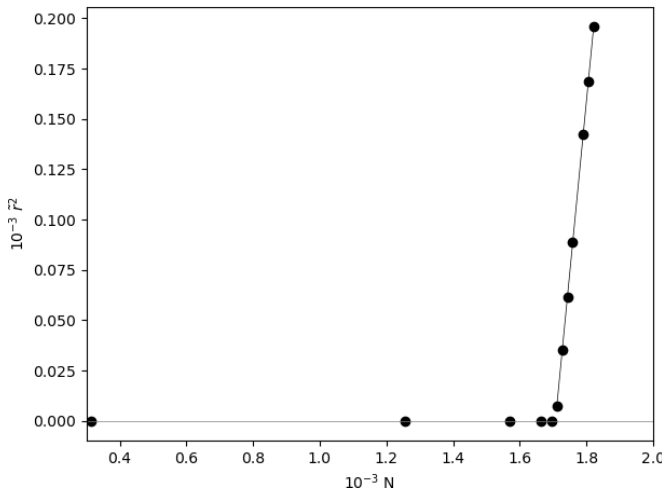


FIG. 15. Bifurcation diagram: Nondimensionalized amplitude of oscillation ( $\tilde{r}^2 = r^2/W^2$ ) vs dimensionless number density ( $N$ ) for  $V_p/W = 0.041$  and  $b/H = 1/3$ .

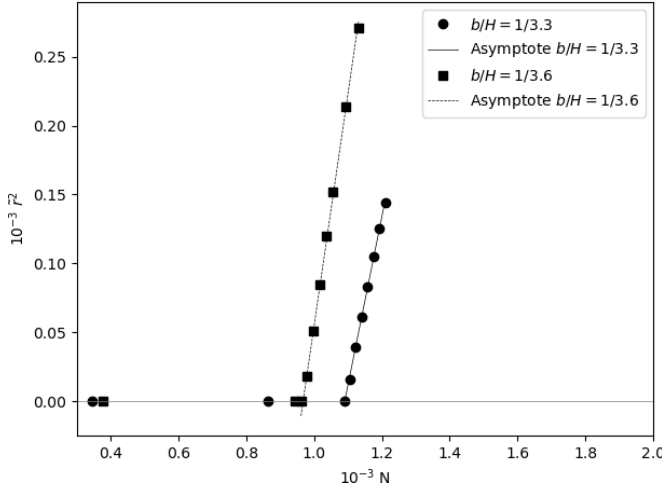


FIG. 16. Bifurcation diagram: Nondimensionalized amplitude of oscillation ( $\bar{r}^2 = r^2/W^2$ ) vs dimensionless number density ( $N$ ) for  $V_p/W = 0.027$ ,  $b/H = 1/3.3$ , and  $b/H = 1/3.6$ .

(Fig. 16) shows that, when  $b/H = 1/3.3$ , the transition occurs near  $N = 1.11 \times 10^{-3}$ . The unstable linear regime has  $N_c = 1.09 \times 10^{-3}$  and  $\alpha = -0.81$ . On the other hand, for  $b/H = 1/3.6$ , the transition occurs near  $N = 0.96 \times 10^{-3}$ ,  $N_c = 0.97 \times 10^{-3}$ , and  $\alpha = -0.61$ . These results, therefore, demonstrate that increasing the print gap height tends to reduce the critical print density as well as increase the sensitivity of the airflow to disturbances.

#### D. Dynamics of frequency

Further investigations on the dynamics of the frequency are performed using the autoregression algorithm. This algorithm has been chosen over the FFT because of the limited resolution of the latter to capture small variations in frequency [25]. Figure 17 displays the impact of number density on the Strouhal number for different printing conditions. For a given  $H/b$  and  $V_p/W$ , the increase

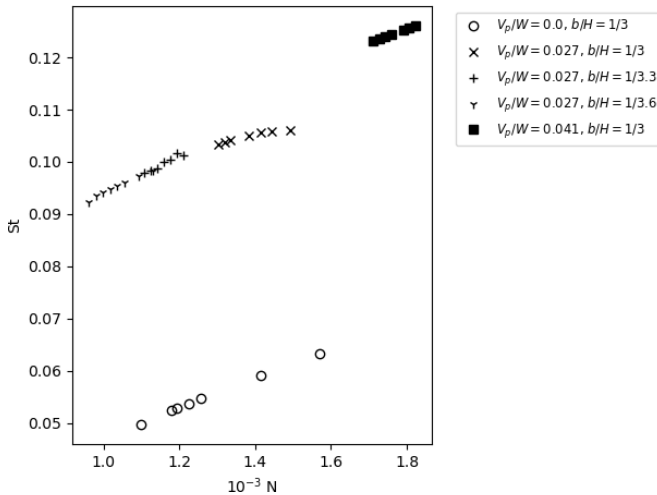


FIG. 17. Strouhal number ( $St = fH/W$ ) vs number density ( $N$ ) for different printing conditions.

in  $N$  tends to slightly increase the fundamental frequency of airflow oscillation. The comparison between systems with same paper speed but different  $H/b$  indicates that higher aspect ratios only tend to lower the Strouhal number because it lowers the  $N$  at which the onset of instability occurs. The driving factor for the Strouhal number is  $N$  since, given the same  $N$ , for instance  $N \approx 1.15 \times 10^{-3}$ , it is observed that the airflow oscillates at the same fundamental frequency even though the systems have different aspect ratios. This demonstrates that, for a constant paper speed,  $N$  is the key parameter for the dynamics of the system, driving the fundamental frequency. This was already expected because  $N$  is the dimensionless number associated to the droplets' body-force [Eq. (7)].

The increase in paper, however, leads to significant variations in Strouhal number. For each paper speed, there exists a specific curve that defines the effect of  $N$  on the frequency of oscillation of the system. The cross-alike markers group the curve for  $V_p/W = 0.027$ , while the filled and hollow markers group  $V_p/W = 0.041$  and  $0.0$ , respectively. This variation also suggests that there is another dimensionless number that characterizes the impact of paper speed and/or volumetric cross-flow on the stability of the airflow.

#### IV. CONCLUSION

Two-dimensional numerical simulations using a dispersed-phase continuum approach to model the entrainment effect of ink droplets were performed to investigate a type of airflow instability in the print gap of inkjet printers and investigate the instability mechanism. The results also indicated that the airflow instability is characterized by sinusoidal oscillations that grow until a saturated amplitude is reached. It was also demonstrated that as the number density increases the flow shifts from stable to unstable at a specific transition point—the critical number density—and the amplitude of oscillation follows an asymptotic square-root behavior, characterizing a supercritical Hopf bifurcation type of instability. For a stationary paper, the transition occurs at a lower critical number density due to the lack of cross-flow which can have a stabilizing effect on the vortices near the injection zone. The stationary paper results, more importantly, indicated that even in the absence of induced cross-flow the airflow can become unstable, contradicting the assertion of previous studies that attributed the mechanism of instability to the interaction between the induced cross-flow and the entrainment effect. The continuous variation in Strouhal number for systems with different print gap height demonstrated that the number density dictates the fundamental frequency of oscillation, while the paper speed variation translates the curve that defines the impact of  $N$  on the frequency of oscillation of the system.

#### ACKNOWLEDGMENTS

We would like to acknowledge Memjet for partially funding this research and the assistance of Dr. D. Stephens, Applied CCM, for assisting with OPENFOAM programming. The numerical analyses were performed in the National Computational Infrastructure high-performance computing facility, which is supported by the Australian Government.

- 
- [1] I. Arango, L. Bonil, D. Posada, and J. Arcila, Prediction of a flying droplet landing over a non-flat substrates for ink-jet applications, *Intl. J. Interact. Design Manufact.* **13**, 967 (2019).
  - [2] *Handbook of Industrial Inkjet Printing*, edited by W. Zapka (Wiley, New York, 2018).
  - [3] *Fundamentals of Inkjet Printing*, edited by S. D. Hoath (Wiley, New York, 2016).
  - [4] S. Wang, Aerodynamic effect on inkjet main drop and satellite dot placement, in *Proceedings of the International Conference on Digital Printing Technologies* (Society for Imaging Science and Technology, 1998), Vol. 1998, pp. 5–9.

- [5] S. G. Mallinson, G. D. McBain, G. D. Horrocks, A. J. North, A. P. O'Mahony, P. J. Reichl, S. J. Myers, J. J. Miller, B. Powell, J. Hess, D. R. Secker, and P. C. Palma, Suppressing tiger stripes: Taming flow oscillations to improve print quality, in *Proceedings of the 20th Australasian Fluid Mechanics Conference* (2016), p. C141.
- [6] S. G. Mallinson, A. D. Aquino, G. D. McBain, G. D. Horrocks, T. J. Barber, C. M. de Silva, and G. H. Yeoh, Three-dimensional numerical simulation of air-flow in inkjet print-zones, *Intl. J. Heat Fluid Flow* **93**, 108911 (2022).
- [7] A. F. V. de Aquino, S. G. Mallinson, G. D. McBain, G. D. Horrocks, C. M. de Silva, and T. J. Barber, Two-dimensional numerical simulation of inkjet print-zone flows, in *Proceedings of the 22nd Australasian Fluid Mechanics Conference AFMC2020*, The University of Queensland (Brisbane, Australia, 2020).
- [8] W. K. Hsiao, S. D. Hoath, G. Martin, and I. M. Hutchings, Aerodynamic effects in ink-jet printing on a moving web, in *Proceedings of the International Conference on Digital Printing Technologies* (Society for Imaging Science and Technology, 2012), Vol. 2012, pp. 412–415.
- [9] C. Rodriguez-Rivero, J. R. Castrejón-Pita, and I. M. Hutchings, Aerodynamic effects in industrial inkjet printing, *J. Imaging Sci. Technol.* **59**, 29 (2015).
- [10] W.-K. Hsiao, G. D. Martin, S. D. Hoath, I. M. Hutchings, M. Hook, and M. Massucci, Evidence of print gap airflow affecting web printing quality, in *Proceedings of the International Conference on Digital Printing Technologies* (Society for Imaging Science and Technology, 2013), Vol. 2013, pp. 303–306.
- [11] N. Link, S. Lampert, R. Gurka, A. Liberzon, G. Hetsroni, and R. Semiat, Ink drop motion in wide-format printers II. Airflow investigation, *Chem. Eng. Process.: Process Intensific.* **48**, 84 (2009).
- [12] D. Lanzerstorfer and H. C. Kuhlmann, Three-dimensional instability of the flow over a forward-facing step, *J. Fluid Mech.* **695**, 390 (2012).
- [13] D. Barnett and M. McDonald, Evaluation and reduction of elevated height printing defects, in *Proceedings of the International Conference on Digital Printing Technologies* (Society for Imaging Science and Technology, 2014), Vol. 2014, pp. 38–43.
- [14] D. Varieras, P. Brancher, and A. Giovannini, Self-sustained oscillations of a confined impinging jet, *Flow, Turbul. Combust.*, 1 (2007).
- [15] V. Goldschmidt and P. Bradshaw, Flapping of a plane jet, *Phys. Fluids* **16**, 354 (1973).
- [16] C.-M. Ho and N. S. Nasseir, Dynamics of an impinging jet. Part 1. The feedback phenomenon, *J. Fluid Mech.* **105**, 119 (1981).
- [17] R. Seydel, *Practical Bifurcation and Stability Analysis* (Springer, New York, 2009).
- [18] F. M. White and I. Corfield, *Viscous Fluid Flow* (McGraw-Hill, New York, 1991).
- [19] T. Holzmann, *Mathematics, Numerics, Derivations and OpenFOAM* (Wiley, New York, 2016).
- [20] R. Fletcher, Conjugate gradient methods for indefinite systems, in *Numerical Analysis*, Lecture Notes in Mathematics Vol. 506 (Springer, Berlin, Heidelberg, 1976), pp. 73–89.
- [21] T. Behrens, Openfoam's basic solvers for linear systems of equations: Solvers, preconditioners, smoothers, 2008, [www.tfd.chalmers.se/~hani/kurser/OS\\_CFD\\_2008/TimBehrens/tibeh-report-fin.pdf](http://www.tfd.chalmers.se/~hani/kurser/OS_CFD_2008/TimBehrens/tibeh-report-fin.pdf).
- [22] T. Gustafsson and G. D. McBain, scikit-fem: A python package for finite element assembly, *J. Open Source Software* **5**, 953 (2020).
- [23] D. K. Gartling, A test problem for outflow boundary conditions: Flow over a backward-facing step, *Int. J. Numer. Methods Fluids* **11**, 2369 (1990).
- [24] P. Drazin, *Introduction to Hydrodynamic Stability* (Cambridge University Press, Cambridge, England, 2002).
- [25] A. Boardman, F. S. Schindwein, and A. P. Rocha, A study on the optimum order of autoregressive models for heart rate variability, *Physiol. Meas.* **23**, 325 (2002).